ELSEVIER

Contents lists available at ScienceDirect

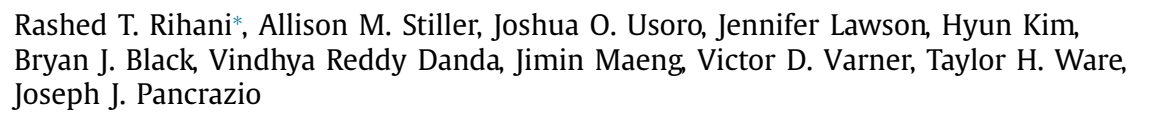
Acta Biomaterialia

journal homepage: www.elsevier.com/locate/actbio



Full length article

Deployable, liquid crystal elastomer-based intracortical probes



Department of Bioengineering, University of Texas at Dallas, Richardson, TX 75080, USA



ARTICLE INFO

Article history: Received 12 February 2020 Revised 13 April 2020 Accepted 17 April 2020 Available online 17 May 2020

Keywords:
Microelectrode array
Neuronal recording
Liquid crystal elastomer
Intracortical probe
Actuating neural interface

ABSTRACT

Intracortical microelectrode arrays (MEAs) are currently limited in their chronic functionality due partially to the foreign body response (FBR) that develops in regions immediately surrounding the implant (typically within 50-100 μm). Mechanically flexible, polymer-based substrates have recently been explored for MEAs as a way of minimizing the FBR caused by the chronic implantation. Nonetheless, the FBR degrades the ability of the device to record neural activity. We are motivated to develop approaches to deploy multiple recording sites away from the initial site of implantation into regions of tissue outside the FBR zone. Liquid Crystal Elastomers (LCEs) are responsive materials capable of programmable and reversible shape change. These hydrophobic materials are also non-cytotoxic and compatible with photolithography. As such, these responsive materials may be well suited to serve as substrates for smart, implantable electronics. This study explores the feasibility of LCE-based deployable intracortical MEAs. LCE intracortical probes are fabricated on a planar substrate and adopt a 3D shape after being released from the substrate. The LCE probes are then fixed in a planar configuration using polyethylene glycol (PEG). The PEG layer dissolves in physiological conditions, allowing the LCE probe to deploy post-implantation. Critically, we show that LCE intracortical probes will deploy within a brain-like agarose tissue phantom. We also show that deployment distance increases with MEA width. A finite element model was then developed to predict the deformed shape of the deployed probe when embedded in an elastic medium. Finally, LCE-based deployable intracortical MEAs were capable of maintaining electrochemical stability, recording extracellular signals from cortical neurons in vivo, and deploying recording sites greater than 100 µm from the insertion site in vivo. Taken together, these results suggest the feasibility of using LCEs to develop deployable intracortical MEAs.

Statement of Significance

Deployable MEAs are a recently developed class of neural interfaces that aim to shift the recording sites away from the region of insertion to minimize the negative effects of FBR on the recording performance of MEAs. In this study, we explore LCEs as a potential substrate for deployable MEAs. The novelty of this study lies in the systematic and programmable deployment offered by LCE-based intracortical MEAs. These results illustrate the feasibility and potential application of LCEs as a substrate for deployable intracortical MEAs.

 $\ensuremath{\mathbb{C}}$ 2020 Acta Materialia Inc. Published by Elsevier Ltd. All rights reserved.

1. Introduction

Implantable intracortical MEAs allow recording and stimulation of neuronal activity within the brain. This capability may enable functional restoration for patients that have suffered limb loss or paralysis [1]. However, the chronic functionality of intracortical MEAs is currently limited, at least in part, by the foreign body re-

* Corresponding author. E-mail address: rxr121330@utdallas.edu (R.T. Rihani). sponse (FBR) that occurs in a 50 to 100 µm range [2–6] around the implant. The FBR consists of astrogliosis and fibrotic encapsulation of the device [7], which may cause neuronal death and expand the physical/electrochemical separation between neurons and recording electrodes [8,9]. The use of low elastic modulus polymer substrates and the design of highly flexible implants with small cross-sectional areas [4,10] have recently been studied for their potential in mitigating FBR-induced encapsulation. Even though alleviating the mechanical mismatch between the device and surrounding neural tissue [11,12] reduces the FBR, it still persists.

Prior work has demonstrated that deployable intracortical probes are capable of extending beyond the FBR zone [10,13-15]. For example, Xie et al. demonstrated a 3D macroporous intracortical probe that contained recording sites on pre-stressed bimetallic strips. The recording sites are kept dormant by freezing in liquid nitrogen, and once implanted, thaw and deploy away from the host shank [16]. In addition, Massey et al. demonstrated a novel architecture for a silicon host shank with small silicon whiskers, intended to contain the recording sites, that splayed outward and away from the FBR zone after implantation [17]. Jiao et al. developed an ultra-flexible and thin intracortical probe attached to a silicon shank using a magnesium sacrificial layer. After implantation, the sacrificial layer dissolved, and the residual stresses in the thin intracortical probe cause it to deploy a small distance away from the shank [14]. These prior studies demonstrated deployable mechanisms, intended to avoid FBR encapsulation. However, none of these approaches enables the deployment of low elastic modulus structures beyond the FBR encapsulation zone (50 to 100 µm).

LCEs, a subclass of liquid crystal polymers, are lightly crosslinked polymers with a low elastic modulus (10 MPa), that can morph from one shape to another [18–20], and have demonstrated biocompatibility *in vitro* [21–23]. Specifically, LCEs that are aligned during crosslinking exhibit reversible shape change when exposed to a stimulus, such as a change in temperature [24,25], light [26,27], electricity [28], or solvent [29,30]. Recently, we have shown that these materials are also suitable substrates for microelectronics processing. This reversible shape change allows LCE-based electronics to "pop-up" into complex 3D shapes even though they are fabricated through 2D planar photolithography [31]. Ultimately, we aim to fabricate LCE-based MEA in which small electrode recording sites can be deployed outside the FBR-induced tissue encapsulation zone at the implantation site, to enable recording from a healthy volume of surrounding neural tissue [2].

Here, we evaluate the feasibility of LCE-based deployable intracortical MEAs. The LCE substrate remains flat during the processing of electronics. Following fabrication, LCE probes are released from the substrate and pop-up into a 3D shape as determined by the alignment of the LCE. These devices are flattened for insertion against a silicon shank using PEG (Fig. S1a). Since flexible probes tend to buckle and bend during insertion, the PEG and silicon shank combination was used as an insertion guide. Dissolvable materials, such as PEG, have been utilized in prior studies to assist with insertion of flexible probes into the brain. Dissolvable materials have also been investigated as a strategy to reduce the FBR, with some studies reporting over 4 months of stable neuronal recordings [32-34]. After implantation, the PEG dissolves and the LCE probe deploys in vivo (Fig. S1b). First, to demonstrate the feasibility of these devices, we characterize the deployment of LCEs of different geometries within a brain phantom gel. We then show select geometries are capable of deployment distances greater than 100 µm within these phantoms. Second, radius of curvature measurements are used to calculate the residual stresses in probes fixed in a planar configuration. These residual stresses drive deployment when the probe is released. A finite element model is then used to predict the deformed (deployed) geometry of different probe designs. Finally, we demonstrate acute neural recordings, short-term electrochemical stability, and in vivo deployment using an LCE-based deployable intracortical probe.

2. Materials and methods

2.1. Fabrication of LCE-based non-functional samples

We fabricated non-functional LCE-based probes to deploy within agarose tissue phantoms (Fig. 1a). LCE-based and silicon non-functional probes were fabricated with varying shank

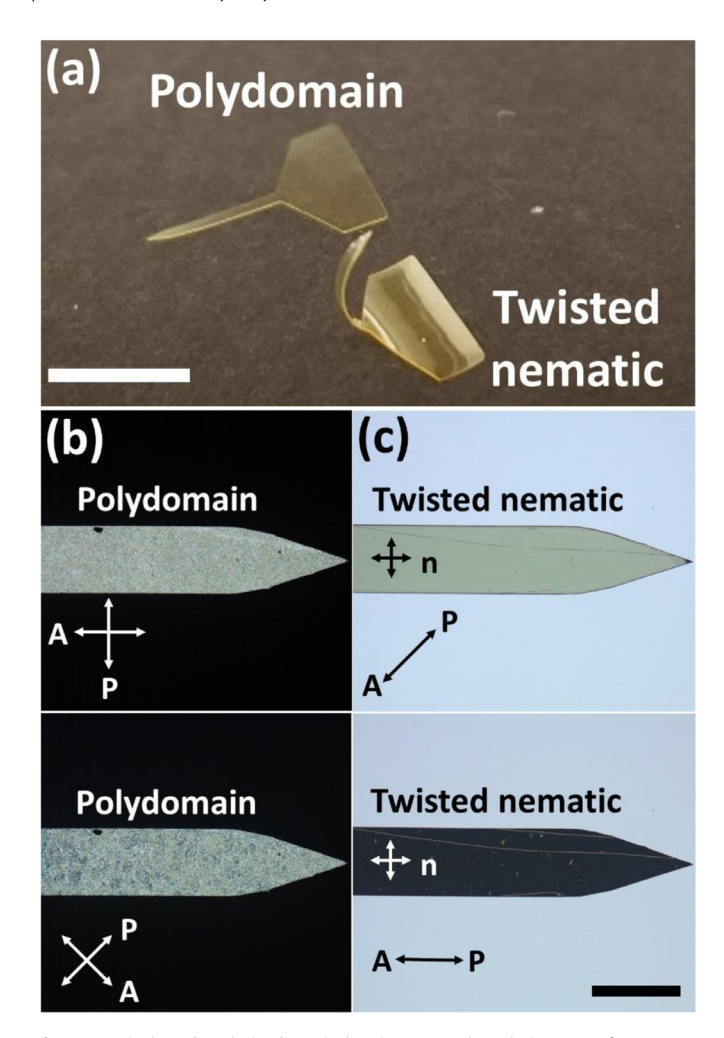


Fig. 1. Optical and polarized optical microscopy (POM) images of LCE nonfunctional probes. (a) Representative optical image of nonfunctional, polydomain and twisted nematic LCE-based probes. Scale bar represents 7 mm. Representative POM images of nonfunctional polydomain (b) and Twisted nematic (c) LCE-based probes. P and A represent the direction of the polarizer and analyzer, respectively. n represents the nematic director of the LCE substrate. Scale bar represents 600 µm.

lengths of 3, 5, and 7 mm and varying shank widths of 0.5, 1, and 2 mm. LCE-based non-functional probes were fabricated through a previously described process [21,24]. Initially, glass slides (75 \times 51 \times 1.2 mm, Electron Microscopy Sciences, Hatfield, PA, USA) were sequentially cleaned with Alconox (Alconox, White Plains, NY, USA)/DI water, acetone, isopropanol, and DI water, then dried with nitrogen. Slides were then exposed to oxygen plasma for 60 s at a pressure of 100 mTorr and power of 50 W using a PX-250 March Asher (Nordson Corporation, Westlake, OH, USA). After slides were cleaned, brilliant yellow (Sigma Aldrich, St. Louis, MO, USA), a photosensitive dye, was mixed with dimethylformamide (DMF, Fisher Scientific, Pittsburgh, PA, USA) to make a 1% wt dye solution. The solution was filtered through a 0.45 µm syringe filter (Whatman, Maidstone, UK) and then spin-coated on the glass slides in two steps. Slides were first spun for 10 s at a speed of 750 rpm and a ramp of 1500 rpm, then for 30 s at a speed of 1500 rpm and a ramp of 1500 rpm. Slides were then photoaligned as previously described [31,35]. Slides were exposed to polarized light (Vivitek D912HD, Vivitek, Fremont, CA, USA) at 0 and 90° with an intensity of 10 mW/cm². Cells for casting LCE were made by placing 35 µm spacers (Precision Brand, Downers Grove, IL, USA) between glass slides with orthogonal alignment. Spacers determined a LCE component thickness of 35 µm.

The LCE mixture was made as previously described [21,24,36]. Briefly, an equimolar amount of 1,4-bis-[4-(6-acryloyloxyhexyloxy)benzoyloxy]-2-methylbenzene (RM82, Wilshire Chemicals, Princeton, NJ, USA) and n-butylamine (Sigma Aldrich, St. Louis, MO, USA) was mixed with 1.5% wt of I-369 photoinitiator (BASF, Ludwigshafen, Germany). The cell was filled with the mixture at 72 °C through capillary action and then stored overnight at 65 °C in the absence of light to allow for oligomerization. The cell was then exposed to 365 nm wavelength ultraviolet light (OmniCure® LX400+, Lumen Dynamics, Mississauga, ON, Canada) at an intensity of 250 mW/cm² and temperature of 92 °C for 2.5 min on each side. Polydomain films were obtained by briefly heating the mixture to 150 °C (isotropic phase) to remove any alignment. The cell was then broken with a razor blade, and the LCE film remained adhered to one glass slide. Alignment of polydomain (Fig. 1b) and twisted nematic (Fig. 1c) LCE films were confirmed using polarized optical microscopy (POM). Polydomain samples were flat when released from the substrate and served as controls for agarose deployment experiments. Twisted nematic samples were aligned at 0 and 90° through the polymer, thus curling when released from the substrate (Fig. 1a).

A silicon nitride hard mask was then deposited at 150 °C on the LCE film using a Plasma Enhanced Chemical Vapor Deposition Unaxis 790 PECVD (Mykrolis Corporation, Billerica, MA, USA). The hard mask was then exposed to hexamethyldisilazane (HMDS, Sigma Aldrich, St. Louis, MO, USA) at 120 °C to improve the adhesion of photoresist to the hard mask. S1813 photoresist (Shipley S1813, Dow Chemical, Midland, MI, USA) was spin-coated onto the substrate at a speed of 2000 rpm and a ramp of 1000 rpm for 45 s. Substrates were subsequently soft baked at 85 °C for 12 min. Substrates coated with photoresist were then exposed to UV light at a dose of 150 mJ/cm² using a Karl Suss MA6 Mask Aligner (SÜSS MicroTec, Garching, Germany). Substrates were developed in Microposit MF-319 (Dow Chemical, Midland, MI, USA) for 45 to 60 s. Silicon nitride was dry-etched (Sirius T2, Trion Technology, Tempe, AZ, USA) through SF₆ plasma at a pressure of 120 mTorr and power of 100 W for about 10 min. The underlying LCE layer was then dry etched through O₂ plasma at a pressure of 220 mTorr and power of 200 W for about 60 min. The substrates were then soaked in 1:10 Hydrofluoric (HF) acid for about 30 s to remove the remaining hard mask from the substrates. Finally, the non-functional devices were released from the substrate by soaking in a 15 wt.% potassium borate solution (AZ400K, AZ Electronic Materials) and then rinsing in DI water.

2.2. Fabrication of silicon non-functional samples

Silicon insertion-guides were fabricated from an SOI wafer using photolithography and plasma etching. SOI wafer with a device thickness of 35 µm was purchased from UltraSil LLC (UltraSil LLC, Hayward, CA, USA). A 1 µm thermal oxide hard mask was deposited onto the SOI wafer. The hard mask was then exposed to hexamethyldisilazane (HMDS, Sigma Aldrich, St. Louis, MO, USA) at 120 °C to improve the adhesion of photoresist to the hard mask. S1813 photoresist was spin-coated onto the wafer at a speed of 2000 rpm and ramp of 1000 rpm for 60 s. The wafer was then soft-baked at 115 °C for 1 min. The wafer was then exposed to UV light through a mask at a dose of 150 mJ/cm². It was subsequently developed in MF-319 for 1 min. The thermal oxide was then dry etched with CHF_3 plasma (gas flow of 40 + 10 sccm for $CHF_3 + Ar$) (PE04, Oerlikon, Pfäffikon, Switzerland) at a pressure of 10 mT and power of $800\ W$ for $450\ s$. The underlying silicon layer was dry etched with SF₆ plasma (gas flow of 20 sccm for SF₆) at a pressure of 10 mT and power of 1200 W using a Bosch process until the buried oxide layer became visible. During this high aspect ratio plasma etching Bosch process, we cycled the wafer through various loops of isotropic etching using SF₆ plasma and fluorocarbon-based protection film deposition using C₄F₈ plasma. Residual photoresist was stripped with acetone, and the wafer was then cleaved into 4 dies using a diamond scribe. A separate carrier wafer (bare silicon) was spin-coated with AZ P4620 (AZ Electronic Materials, Luxembourg) at a speed of 2000 rpm and ramp of 1000 rpm for 60 s. One of the above 4 dies was then placed upside down onto the coated carrier wafer and placed on a hot plate at 135 °C. A 5 lb weight was placed on top of the wafer and die combination for 35 min to create a seal. The backside of the die, still on the carrier wafer, was dry etched as seen above with CHF₃ for 450 s to remove residual thermal oxide. The underlying silicon layer was then dry etched using the same Bosch process as above until silicon is no longer visible. The die and carrier wafer were soaked in AZ400T for 30 min at 70 °C until the probes released from the die. The released probes were cleaned again with AZ400T and DI water to remove any residual photoresist. Probes were then soaked in 49% HF for 2 min to etch the buried oxide layer and then rinsed thrice with DI water. This process was repeated for each of the remaining 3 dies.

2.3. Residual stress measurements of flattened LCE strips

Thin, rectangular LCE strips, fabricated as described above, adopt a curled geometry at room temperature when left unconstrained. In a flattened configuration, the strips are no longer stress-free and experience residual bending stresses that vary across the thickness of the sample. The maximum stresses occur along the top and bottom surfaces, with one surface in tension and the other in compression. Because of this, the strip returns to a curled geometry when free of any external mechanical constraints. Upon implantation, the stored residual stresses will drive the deployment of the LCE probe. Thus, to quantify the residual stresses in flattened LCE strips, we measured the radius of curvature of each strip in its (zero-stress) curled configuration. The following rectangular probe geometries were used: 3 mm by 2 mm, 3 mm by 1 mm, and 5 mm by 2 mm. Side view images were captured using a horizontally mounted digital camera, and a custom ImageJ (NIH) macro was used to calculate the radius of curvature of each curled LCE strip. We then used the following equation to relate the measured radius of curvature to the magnitude of the maximum bending stress in the flattened LCE strip, assuming both linear elastic material behavior and a (constant) rectangular crosssectional area [37]:

$$\sigma = \frac{EH}{2\rho} \tag{1}$$

where ρ is the radius of curvature, E represents the elastic modulus, H is the thickness of the LCE strip, and σ represents the magnitude of the maximum bending stress. The computed stresses were then compared to those predicted by finite element models of LCE strip unbending, as described below.

2.4. Agarose deployment tests

LCE and silicon probes without patterned electronics were assembled, as seen in Fig. 3a. Polyethylene glycol 1000 g/mol (PEG, Alfa Aesar, Massachusetts, USA) was melted and applied to the two probes. The non-functional LCE-based probe was placed on top of a silicon probe (covered in PEG) of the same dimension and heated using a hot plate (50 °C), which caused the probe to flatten to an undeployed state. On cooling the PEG crystallizes and holds the LCE probe in a planar state. Agarose hydrogels (0.2 wt%) at 37 °C were used as a brain phantom [38,39] for deployment testing. To measure deployment, side view images as seen in Fig. 3a were taken using a MicroSquisher (CellScale, Waterloo, ON, Canada). To

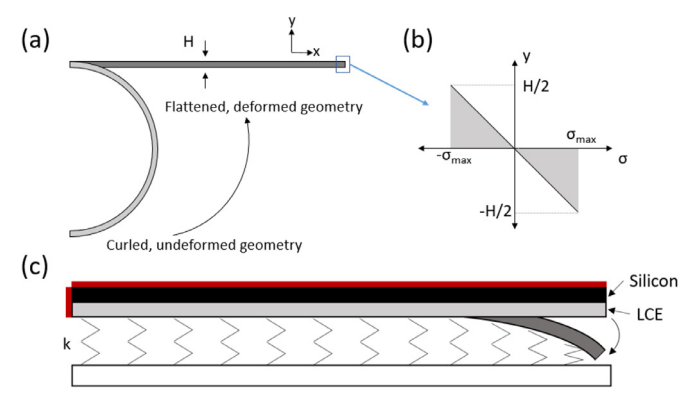


Fig. 2. Finite element analysis models to investigate LCE curling. (a) An LCE sample was modeled in the curled, undeformed geometry (light gray) and uncurled into a deformed geometry (dark gray) with prescribed displacements. The dimension 'H' refers to the thickness of the strip. (b) When in the flattened geometry, the LCE sample exhibits a stress distribution that varies across the thickness ($H=35~\mu m$) of the strip. (c) An LCE strip is fixed to a silicon ($H=35~\mu m$) backing (black) to mimic the deployment testing setup. The LCE is given an initial stress concentration as seen in (b) with appropriate σ_{max} values derived from (a) which causes the strip to move from the flattened geometry (light gray) to the curled geometry (dark gray). The bottom of the LCE strip is restrained by linear elastic springs with spring constant, k, to oppose the displacement of the tip. The red lines on the upper and left boundaries of the silicon indicate fixed boundary conditions. The same coordinate system in (a) applies to (c).

initiate deployment, the non-functional probe was inserted into agarose gel at 37 °C. On insertion, the PEG layer dissolved and the device deployed. The distance between the tip of the silicon probe and the tip of the LCE-based probe was used to quantify the deployment distance (n=3). The deployment distance was defined as the initial distance between the tips subtracted from the final distance between tips, measured 60 s after insertion.

2.5. Mechanical modeling of deployable LCE strips

COMSOL Multiphysics[®] v 5.4. (COMSOL AB, Stockholm, Sweden) software was used to create a finite element model of the deployable LCE strips. All model geometries were based on the rectangular probe dimensions specified in Section 2.2. LCE was assumed to exhibit isotropic, linear elastic material behavior with an elastic modulus of 10 MPa, density of 1300 kg/m³, and Poisson's ratio of 0.49.

First, to confirm the residual stresses computed using Eq. (1), we created a 2D (plane stress) model for each strip in its initial, curled configuration. (This configuration represents the strip in its undeformed, zero-stress state.) We then prescribed displacements within the model to flatten the strip and computed the resultant bending stresses (Fig. 2a). Specifically, we analyzed stress at the outer edges of the strip thickness and took the average as the maximum bending stress. The computed stresses were compared to the values obtained using Eq. (1).

Then, to compute the deformed shape of the deployed probe, we created a model of the flattened LCE strip affixed to a silicon shank and embedded within an elastic medium. The model was used to simulate the deployment of an LCE strip away from a silicon shank when implanted in a 0.2% agarose gel. The residual stresses computed using Eq. (1) were specified across the thickness of the flattened LCE strip (Fig. 2b) and caused the probe to bend away from the silicon shank (Fig. 2c). The surrounding agarose was modeled as a foundation of linear elastic springs distributed along the length of the probe to mimic the mechanical constraint of the surrounding gel during probe deployment. We assumed a spring constant per unit length of 1000 N/m² or 1 kPa [40,41] to approximate the mechanical behavior of 0.2% agarose. The model was also

used to estimate the force of LCE deployment by integrating stress in the y-direction over the length of the LCE/spring boundary interface and multiplying the resulting value by the thickness of the sample.

2.6. Fabrication of functional LCE-based devices

Based on the agarose deployment results, a shank length of 5 mm and width of 2 mm was selected for functional, 8 channel LCE-based deployable probes. LCE films were cast on glass slides as described above. A 400 nm layer of gold was deposited through e-beam evaporation (Temescal BJD-1800, Ferrotec Corporation, Livermore, CA, USA). To pattern the metal traces, S1813 photoresist was spin-coated, baked, exposed to UV light through a mask, and developed as described above. The gold layer was then wet etched with a gold etchant (Transene Company, Midland, MI, USA) for about 1 min. The residual photoresist was then removed through a blank exposure to 150 mJ/cm² of UV light and subsequent soaking in MF-319 developer. A 2 µm layer of Parylene-C (Specialty Coating Systems, Indianapolis, IN, USA) was then deposited to provide a thin and sufficient amount of insulation that would still allow LCE actuation. To open the electrode sites and pads, \$1813 photoresist was spin-coated, baked, exposed to UV light through a mask, and developed as described above. Parylene-C was then dry etched using O2 plasma at a pressure of 100 mTorr and power of 100 W for about 14 min or until 60 µm diameter sites were exposed. A silicon nitride hard mask was deposited, patterned, and etched as previously described. The underlying LCE layer was dry etched as previously described, and the silicon nitride hard mask was etched using 1:10 HF for 30 s. Prior to releasing functional LCE-based devices, the substrate was blanket-etched through O2 at a pressure of 220 mTorr and power of 200 W for 30 s to clean organic residue from the electrode sites and contact pads. Subsequent characterization of the surface (Veeco Dektak VIII profilometer, Veeco, Plainview, New York, US) revealed a minimal 0.1 µm loss of Parylene-C. LCE-based probes were released from the glass slide and assembled similarly to the non-functional LCE-based probes. Devices were inserted into Zif-Omnetics connectors that were donated by Qualia Labs Inc. (Qualia Labs Inc., Richardson, TX, USA), as seen in Fig. 6a. Devices set aside for acute in vivo experiments were imaged as described above to record the initial distance between the shank tips (Fig. 8a).

2.7. Electrochemical characterization of functional LCE-based devices

All functional devices were characterized through electrochemical impedance spectroscopy (EIS) in a 3-electrode set up (counter, reference, and working) in phosphate buffered saline (PBS). The electrochemical integrity of devices (n=8) was tested in three conditions: in the released state, assembled in the planar state, and after deployment.

Two devices (n=16) were set aside for a 7-day soak test. LCE-based functional probes, platinum counter, and Ag|Ag/Cl reference were sealed in a cell using silicone. The cell was filled with PBS until the electrodes were submerged and then placed in a water bath at 37 °C. EIS measurements were taken daily for 7 days with fresh PBS replaced daily.

2.8. Implantation and recording of functional LCE-based devices

2.8.1. Surgical implantation

All procedures performed were approved by the Institutional Animal Care and Use Committee at the University of Texas at Dallas. The surgical methods used were similar to those outlined by Stiller et al. [42]. Briefly, adult, male Long Evans rats (n = 2 animals) were anesthetized using 3–5% isoflurane and given an in-

traperitoneal injection of a 65 mg/ml ketamine, 13.3 mg/ml xylazine, 1.5 mg/ml acepromazine cocktail. Rats were then administered a 0.05 mg/kg intramuscular shot of atropine sulfate. The implantation site was then shaved and cleaned, and the rat was placed in a stereotactic frame (Kopf 940, Kopf Instruments, Tujunga, CA, USA) supplied with a constant supply of 1-2% isoflurane mixed with 100% oxygen. A midline incision was made, and the temporalis muscles and periosteum reflected to expose the skull. Two bone screws were placed in the skull to provide sites for the stainless steel reference and ground wires of the array. A craniotomy was made above the left motor cortex, and the meninges were resected to allow for implantation. Devices were implanted in a craniotomy (\sim 2 \times 3 mm) centered around 2 mm lateral and 2 mm anterior relative to the bregma (left rostral). Exact implantation coordinates within the craniotomy varied slightly from animal to animal depending on the presentation of surface vasculature. The LCE-based array was then inserted into the brain at 1000 µm/s (Kopf 940, Kopf Instruments, Tujunga, CA, USA) to a depth of approximately 3 mm. The deployment time in brain tissue is expected to be similar to that of the agarose brain phantom, therefore neural recordings began 60 s after implantation. Following the neural recording, rats were sacrificed using a 200 mg/kg intraperitoneal injection of sodium pentobarbital.

2.8.2. Electrophysiological recording and analysis

Immediately following implantation and deployment of the device, neural recordings were performed while the animal remained under anesthesia as detailed in Black et al. [43]. Wideband data were recorded simultaneously from all 8 channels at a sampling frequency of 40 kHz for 10 min (Omniplex, Plexon, Dallas, TX, USA). Data were then processed in Plexon's PlexControl software using a 4-pole, low-cut, Butterworth filter with a cutoff frequency of 250 Hz. Single-unit activity was discriminated using a -4σ threshold based on the root mean square (RMS) noise for each respective channel. Following thresholding, single units were manually sorted based on cluster separation in two-dimensional principal component (PC) space. Signal-to-noise ratio (SNR) was calculated as the ratio of peak-to-peak voltage (Vpp) of unit activity to RMS noise. Additional analysis was carried out through NeuroExplorer (Nex Technologies) software and custom MATLAB scripts.

2.9. In vivo deployment

Immediately after neuronal recording, rats were intraperitoneally administered 200 mg/kg sodium pentobarbital. Rats were fixed as previously described [42]. Briefly, 500 ml of PBS was transcardially perfused through the animal, followed by 500 ml of 4% Paraformaldehyde. The brain was separated from the skull and placed in paraformaldehyde overnight. The brain was then sliced into approximately 3-4 mm thick slices so that the electrode remained intact with the surrounding tissue. The tissue slices containing the device were cleared as previously described [44]. Pilot studies were conducted on control tissue slices to optimize the clearing protocol. Briefly, slices were dehydrated in increasing concentrations of methanol in PBS. Slices were dehydrated at concentrations of 25% for 7 hrs, 50% for 5 hrs, 75% for 12 hrs, and 100% for 23.5 hrs. Refractive indices of the tissue and clearing solution, Murrays Clear (1:2 ratio of benzyl alcohol to benzyl benzoate), were matched in a custom made imaging well. Brightfield images were taken using an Axio Imager 2 microscope (Carl Zeiss AG, Oberkochen, Germany).

2.10. Statistical analysis

All statistical analysis was completed using OriginPro software (Origin Labs, Northampton, MA, USA). All values are reported as

mean \pm SEM unless otherwise stated. In the case of agarose deployment tests, treatment groups were compared using a two way ANOVA. In the case of electrochemical impedance spectroscopy, a one way ANOVA or paired t-test was used to compare treatment groups. In all cases, p<0.05 was considered to be statistically significant. One asterisk denoted p<0.05, and two asterisks denoted p<0.01.

3. Results

Here, we evaluate the feasibility of developing and fabricating LCE-based deployable intracortical probes. Initially, we determined residual stresses based on radius of curvature measurements. A finite element model was developed from this data to predict the deformed probe state when inserted in a brain phantom. Second, we use nonfunctional LCE-based intracortical probes to characterize deployment as a function of shank width and length within 0.2% agarose. Finally, we use a functional LCE-based deployable intracortical probe to evaluate short-term electrochemical stability, record neuronal signals from the motor and medial orbital cortex of Long Evans rat, and demonstrate *in vivo* deployment greater than 100 µm.

3.1. Fabrication of LCE-based nonfunctional probes and agarose deployment tests

To develop deployable LCE-based intracortical probes, both polydomain and twisted nematic LCE-based nonfunctional probes (Fig. 1a) were successfully fabricated using photolithography. For twisted nematic LCEs, the photoalignment layer of the first slide was aligned at 0° and the second slide at 90°, causing the nematic director (molecular orientation) of the LCE to rotate through the thickness of the film. As these materials in the cell are crosslinked at elevated temperature, this imprinted twisted nematic configuration allowed the probes to release from the slide in a deployed (curled) state. On the other hand, polydomain samples were unaligned and thus flat when released from the slide. More specifically, twisted nematic samples bent along the long axis of the film with the side of the director oriented along the long axis of the film forming the outside of the bend as previously shown [45]. POM images of the samples revealed alignment in twisted nematic samples (Fig. 1b) and the lack of alignment in polydomain samples (Fig. 1c).

Twisted nematic nonfunctional LCE-based intracortical probes are capable of deployment greater than 100 µm in a 0.2% agarose brain phantom (Fig. 3). LCE-based probes (polydomain and twisted nematic) of multiple shank widths and lengths were adhered to silicon shanks of similar sizes using a thin PEG layer to bring them to their flat or undeployed state. Once the LCE/PEG/Silicon shank was inserted into 37 °C agarose, the PEG melted and dissolved, allowing for deployment. Polydomain samples were used as controls. Images were taken After insertion into the phantom, observed deployment distances were no greater than 7 μ m (n = 3) from the silicon shank (Table S1). Twisted nematic deployment distances varied between 135 and 351 μ m (n = 3), based on the geometry of the probe. As the width of the probe increased, the deployment distance increased significantly at every selected length (Fig. 3c). As a function of length, deployment distance changed in no particular trend at every selected width (Fig. 3b). Overall, changing length only produced a significant effect in 2 of the iterations, suggesting that this metric did not have a consistent effect on LCE deployment distance. In addition, the significant effects seen in these two iterations were observed at the highest aspect ratio. Changing width produced a significant effect in all of the iterations, suggesting that this metric had a consistent effect on LCE deployment

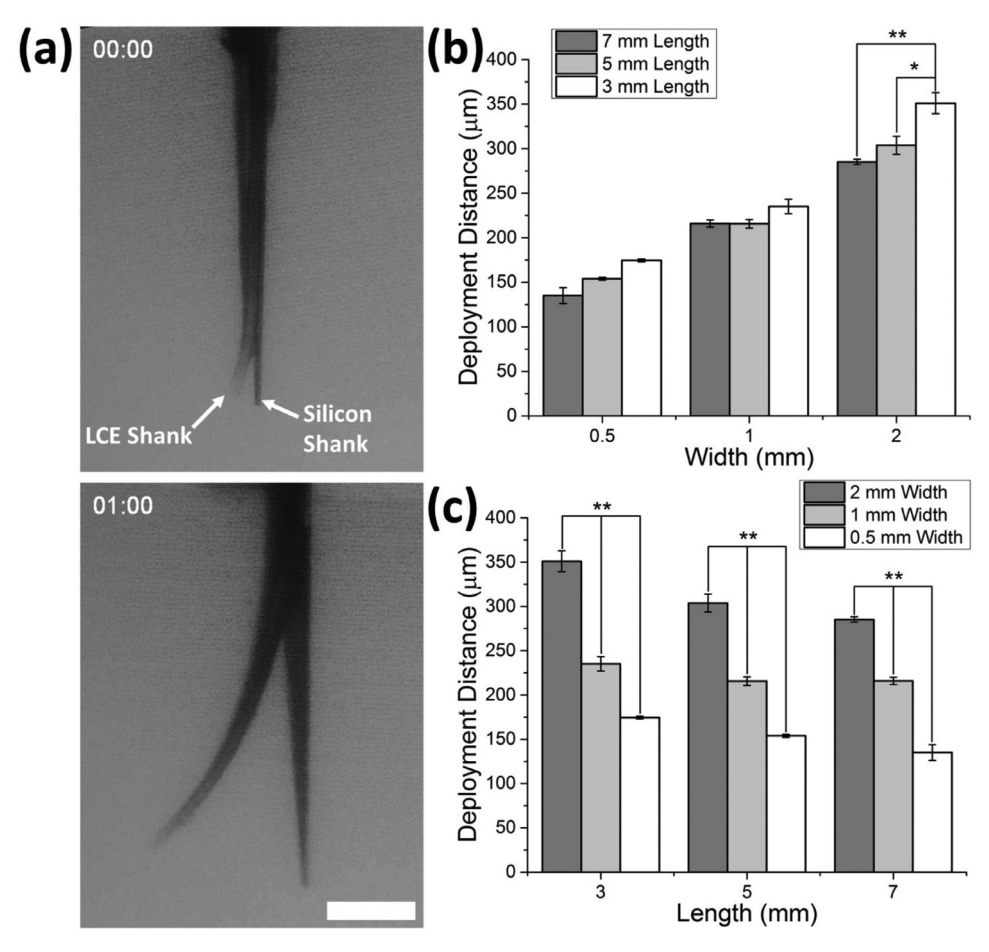


Fig. 3. 0.2% agarose deployment testing. (a) Representative image of the tip of LCE-based deployable non-functional probe at 0 s (top) and 60 s (bottom) after insertion. Scale bar represents 300 μm. (b) Effect of different shank lengths on deployment distance of LCE-based deployable non-functional probes. (c) Effect of different shank widths on deployment distance of LCE-based deployable non-functional probes.

distance and appeared to be the dominant factor. Notably, the deformation primarily occurs within 500 to 1000 μm from the tip of the device.

3.2. Bending curvature and modeling results

We sought to develop a finite element model to provide insight into the deployment of LCE probes in a brain mimic. The curling behavior of LCE strips with varying widths and lengths was observed, and the resulting radius of curvature (ρ) was measured (Fig. 4a and b). These values were then used to estimate the magnitude of the maximum bending stresses in the flattened LCE probes ($\sigma_{\rm max}$) using both Eq. (1) as well as a finite element model of LCE probe flattening (Fig. 4c). We computed similar residual stresses using both of these methods (Fig. 4d), suggesting that although LCEs exhibit anisotropic mechanical properties, the simple material assumptions employed in the model (linear elastic and isotropic) were adequate to predict the bending behavior of thin LCE strips.

Out of the three geometries tested, the LCE strip with a length of 3 mm and a width of 2 mm exhibited the largest maximum bending stress using either Eq. (1) (211.3 \pm 6.4 kPa) or the model (239.1 kPa). The strip with a length of 3 mm and a width of 1 mm exhibited the lowest maximum bending stress with Eq. (1) (125.7 \pm 2.5 kPa) and the model (136.4 kPa). Of the geometries analyzed, we observed an inverse dependence between the magnitude of the maximum bending stress and the aspect ratio of the LCE strip (Fig. 4d). Computational modeling also revealed

a similar inverse dependence between deployment force and aspect ratio. We estimate that the L3W1, L3W2, and L5W2 LCE strips would have deployment forces of 68 μ N, 213 μ N, and 135 μ N, respectively.

The computed residual stresses were then prescribed as initial conditions in a different model to predict the deformed shape of each deployed strip when embedded in a 0.2% agarose tissue phantom (Fig. 5a). The predicted tip displacements were compared to those measured in our agarose deployment tests (Fig. 5b). As observed experimentally, the deflection was localized to the tip of the LCE strip owing to the mechanical constraint of the spring foundation. This effect is in good agreement with what was observed during the agarose deployment tests (Fig. 3a), indicating that the model provides interesting insight regarding the mechanics of deployment despite assumptions regarding the material properties of both the springs and the LCE strips. We also observed a correlation between the magnitude of the maximum bending stress and computed tip displacement, suggesting that probe geometries with higher residual stresses in the flattened configuration will deploy greater distances.

3.3. Electrochemical stability of functional LCE-based devices

The 5 mm long and 2 mm wide design was selected for further studies because it was one of the designs that deployed furthest in agarose. After the fabrication of functional LCE-based deployable probes (Fig. 6a), the electrochemical stability of the devices was demonstrated following shape change. The devices were

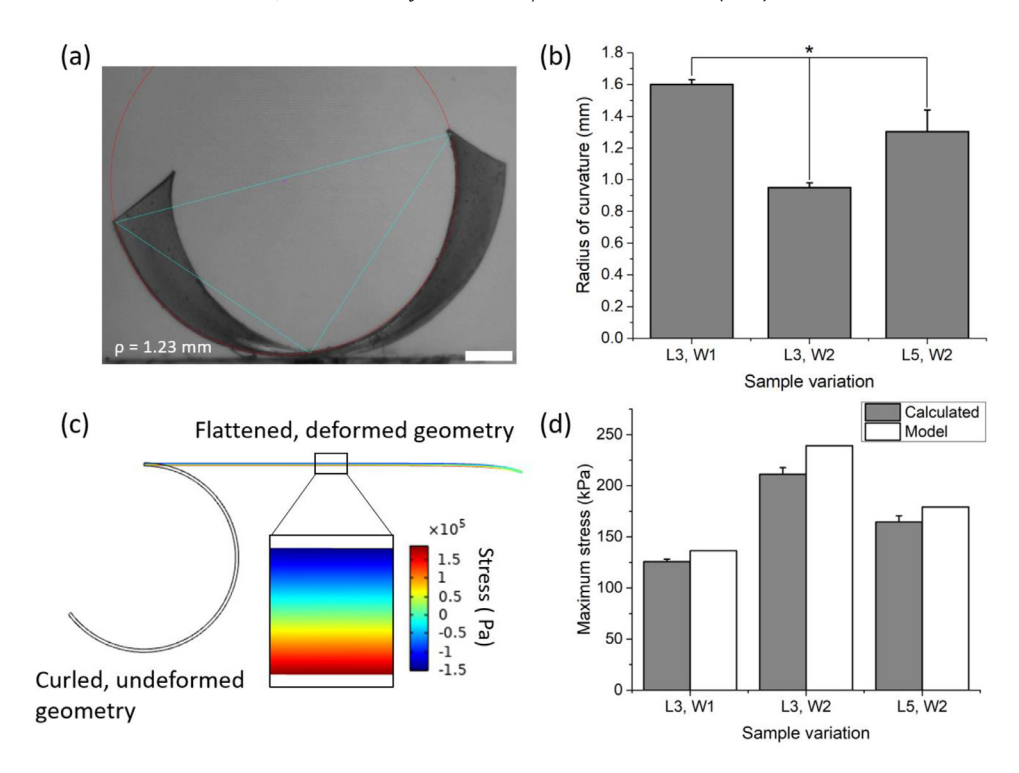


Fig. 4. Radius of curvature and stress measurements. (a) Representative optical image of an LCE strip (L5, W2) in the curled geometry. The blue and red lines in the optical images were drawn in Image] to perform radius of curvature measurements. Scale bar represents 300 μm. (b) Graphical representation of measured radius of curvature for all strip geometries. The numbers following 'L' and 'W' indicate length and width, respectively, in mm. (c) Representative result of one strip (L5, W2) after being flattened from its curled geometry. The inset in the black box depicts the stress distribution across the device thickness where the top edge is in compression and the bottom edge is in tension (indicated by positive and negative stress values, respectively). (d) Graphical representation comparing maximum stress values calculated using Eq. (1) and measured using the model. (For interpretation of the references to color in this figure legend, the reader is referred to the web version of this article.)

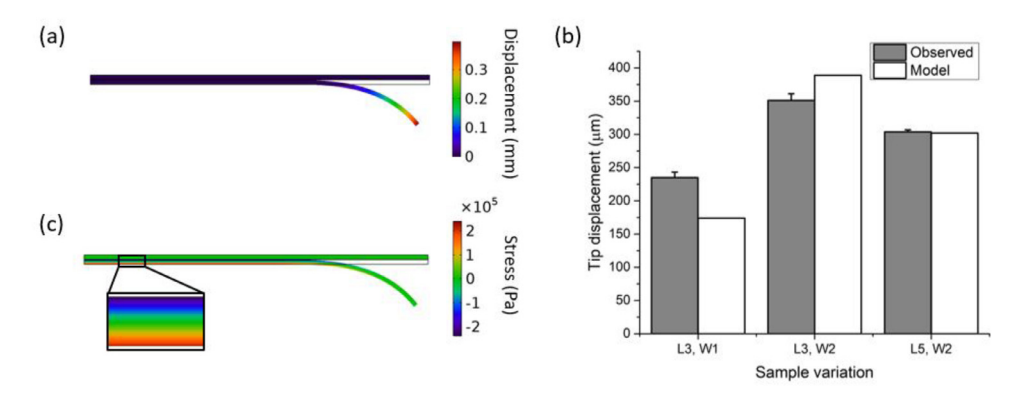


Fig. 5. Comparison of observed and model results of LCE strip deployment. (a) Representative model results for the L5 W2 geometry where the color bar indicates displacement magnitude in mm. (b) Graphical representation of tip displacement observed in the agarose tests compared to that observed in the model. All observed values for each sample variation were significantly different from each other as reflected in Fig. 3. (c) Representative stress distribution in the L5 W2 geometry after deployment (color bar indicates stress in Pa).

also exposed to PBS for 7 days at 37 °C to demonstrate their electrochemical stability under acute conditions. As shown in Fig. 6b, the impedance magnitude at 1 kHz did not change significantly (one way ANOVA, Tukey's, $p=0.21,\ n=8$) as the probe went from a curled (deployed) state (404 k $\Omega\pm11.8$), to a flat state (425 k $\Omega\pm6.5$), and back to a curled state (419 k $\Omega\pm4.7$). Likewise, the phase at 1 kHz did not change significantly (one way ANOVA, Tukey's, $p=0.62,\ n=8$) as the probe went from a curled state ($-73^{\circ}\pm0.84$), to a flat state ($-74^{\circ}\pm0.57$), and back to a curled state ($-74^{\circ}\pm0.62$) (Fig. 6c). These results suggest that the device insulation, conductors, or electrodes were not significantly altered by shape change.

To evaluate the short-term electrochemical stability of these devices, 2 devices were aged at 37 °C in PBS for 7 days (Table S2). The

initial impedance magnitudes at 1 kHz of the electrodes ranged from 285 to 607 k Ω on day 0 and averaged to 436 \pm 102.7 k Ω (mean \pm SD). The final impedance magnitudes at 1 kHz of the electrodes ranged from 157 to 271 k Ω on day 7 and averaged to 215 \pm 36.6 k Ω (mean \pm SD). While significantly lower (p<0.05, n = 16), this change was mainly attributed to an initial decrease seen in days 0–4. In fact, there was no significant difference in the impedance magnitude at 1 kHz between days 4 and 7 (paired t-test, p = 0.1, n = 16). Likewise, there was no observable effect on the phase at 1 kHz, which started at -74 \pm 0.67° on day 0 and ended at -78 \pm 0.37° Again, there was no significant difference in the phase at 1 kHz between days 4 and 7 (paired t-test, p = 0.24, n = 16). Overall, the impedance magnitudes at 1 kHz through 7 days were still well within the range of values capable of record-

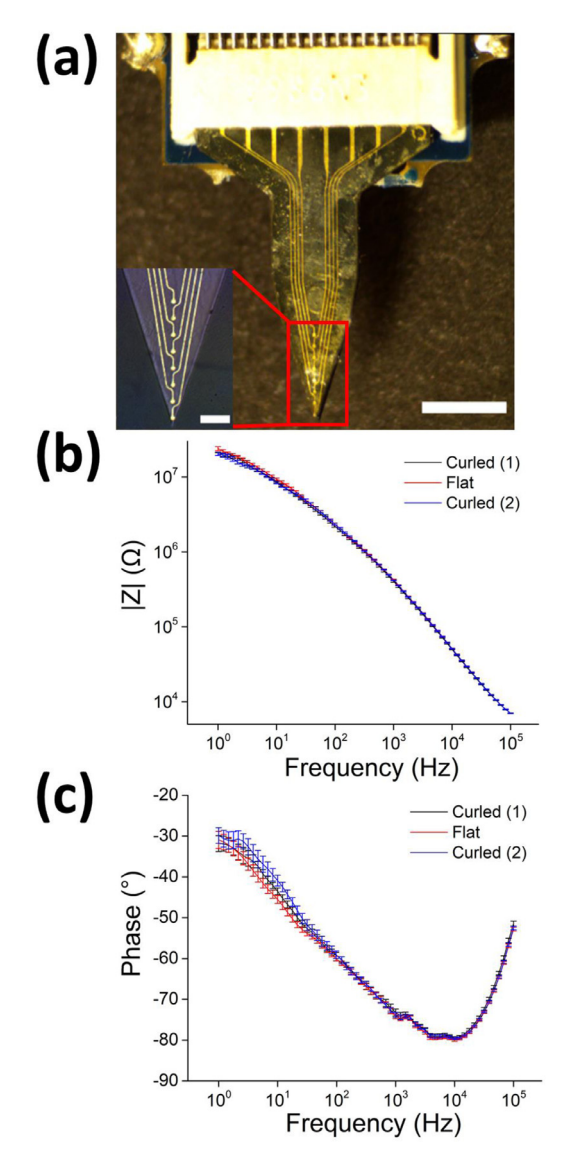


Fig. 6. Electrochemical characterization of functional LCE-based deployable devices. (a) Functional LCE-based deployable device. Scale bar represents 2 mm. Inset shows LCE recording sites, spaced 260 μ m apart. Inset scale bar represents 500 μ m. (b) ElS magnitude and (c) phase of a functional LCE-based deployable device as it transitions from a deployed (curled (1)) state, to an undeployed (flat) state, and back to a deployed (curled (2)) state.

ing neural signals [46,47], suggesting that these devices were sufficiently electrochemically stable for acute *in vivo* studies.

3.4. In vivo electrophysiological recording and deployment

LCE-based deployable intracortical probes were used to record neuronal signals from rat motor cortex. Eight-channel, LCE-based functional devices were implanted into Long-Evans rat motor cortex (Fig. 7a) (n=2 animals), a region abundant in spontaneously firing neurons [42,43], and allowed to deploy by waiting 1 min. LCE-based functional probes were capable of acquiring band pass-filtered extracellular recordings (Fig. 7b). The mean SNR recorded was 13.3 ± 2.9 , and single units were detected on $56.3 \pm 4.4\%$ of the electrodes. In some cases, more than one single unit was detected on a single electrode (Fig. 7d). Spikes were sorted using PC analysis and were separated based on clusters (Fig. 7c), representing multiple neuronal sources. These results suggest that LCE-

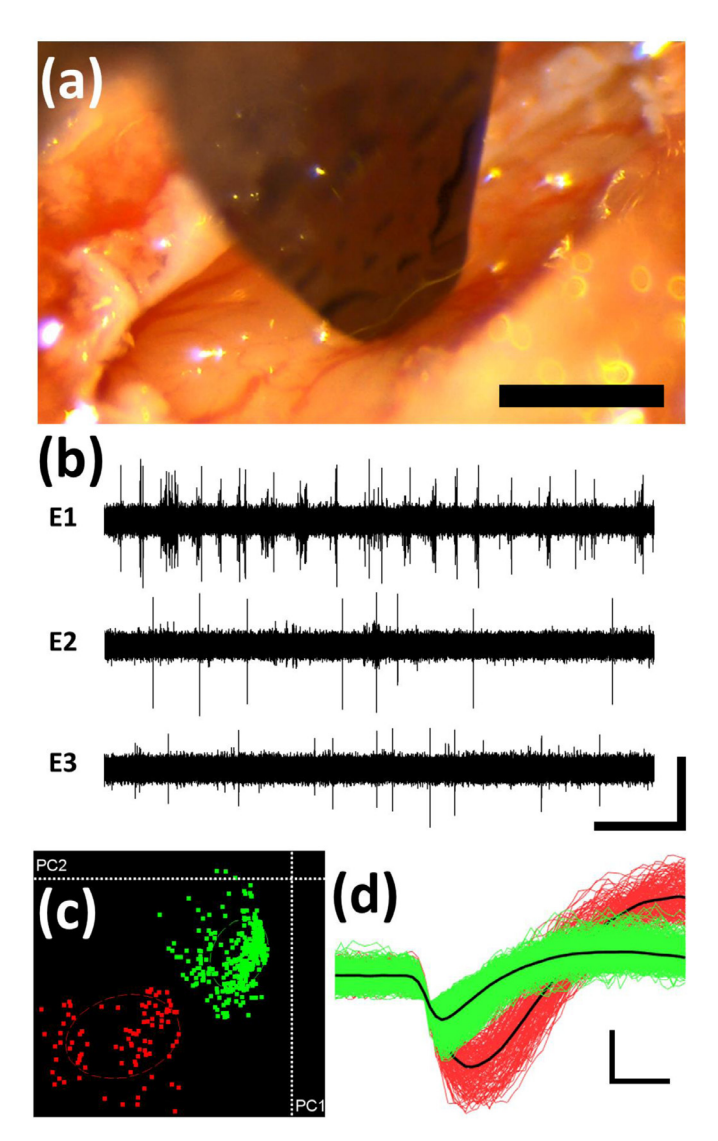


Fig. 7. Overview of acute electrophysiological recordings from functional LCE-based deployable devices. (a) Implantation of functional LCE-based deployable device (tip of silicon side shown) into rat motor cortex. Scale bar represents 1 mm. (b) Representative bandpass-filtered extracellular continuous recordings from 3 electrodes. Vertical and horizontal scale bars represent 40 μv and 5 s, respectively. (c) PC analysis of waveforms recorded from functional LCE-based deployable device. (d) Representative extracellular waveforms recorded from functional LCE-based deployable device. Vertical and horizontal and scale bars represent 20 μv and 200 μs, respectively.

based devices could successfully record distinct neuronal signals in acute conditions from rat cortex.

To ensure that the LCE probe had deployed *in vivo*, the neural tissue containing the device was fixed, cleared, and imaged. The clearing process produced minimal tissue shrinkage, showing only a 4–7% percent change in volume. The deployment distance of the LCE probe with respect to the silicon shank was measured to be 579.9 μ m and 472.5 μ m (n=2 animals), suggesting that the LCE-based deployable probe was capable of deploying greater distances than those associated with FBR (50–100 μ m) (Fig. 8b).

4. Discussion

In this study, we demonstrated the feasibility of LCE-based deployable intracortical MEAs and showed deployment distances greater than 100 µm *in vivo*. The salient feature of these novel devices is that the programmable shape-changing behavior of LCEs

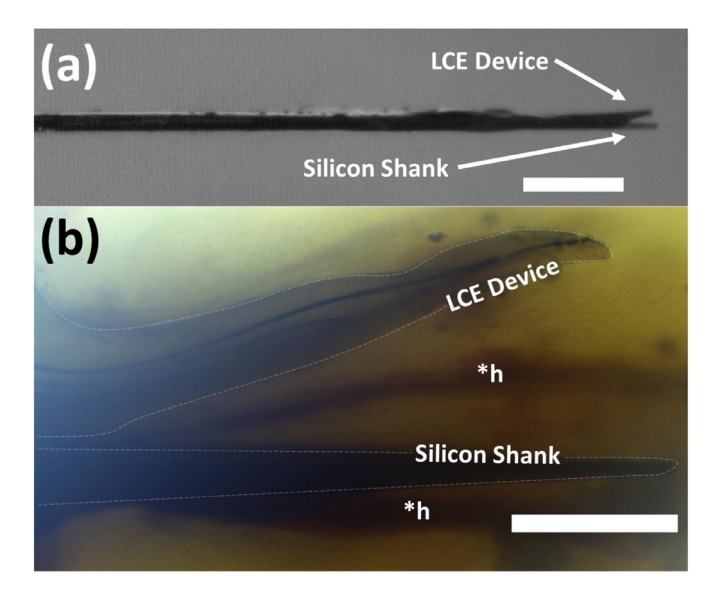


Fig. 8. Functional LCE-based deployable device deployment *in vivo.* (a) Functional LCE-based deployable device prior to insertion. Scale bar represents 300 μm (b) Functional LCE-based deployable device in clear brain tissue after implantation. Scale bar represents 500 μm. *h represents residual heme left after clearing.

can be used to create elastomeric MEAs that deploy within a 3D volume after implantation. To evaluate the deployment capability of LCEs for deployable MEAs, nonfunctional twisted nematic LCEbased probes of different sizes were attached to a size-matched silicon host shank using PEG and inserted into a 0.2% agarose brain phantom. The PEG layer was applied manually, and the unevenness of the layer caused rough bumps and the appearance of minimal delamination at the tips of the device. Since we measured deployment distance as the difference between the final and initial location of the tips, this particular issue did not affect the interpretation of our reported results. The silicon host shank used in this study served a dual purpose. It 1) acted as an insertion guide for the soft LCE-based device and 2) served as a fixed reference point from which to measure LCE deployment. As the width was increased for a shank of a given length, the deployment distance significantly increased. For shanks of a fixed width, as the length was increased, there was no consistent significant effect on the deployment distance. In other words, width was the dominant factor impacting deployment distance. The ability to design shanks of different length while maintaining similar deployment distances is highly advantageous since this could allow for access to deeper structures in the brain (i.e., hippocampus or thalamus) or structures farther from the host shank. Importantly, regardless of length, we observed deployment distances greater than 100 μm, indicating sufficient deployment to avoid the FBR zone. Specifically, the shank tested in vivo deployed over 500 µm. Furthermore, deployment distances in agarose testing were also observed in the model outcomes indicating that the model may be a useful tool with regard to future designs. While only three iterations were tested here, the model could be used to investigate the impact of aspect ratio on predicted tip displacement. For example, targeting different tissue structures or volumes will require the use of a device with different geometries and the model may help determine the minimum width increase required to achieve the desired deplovment.

While it is paramount that the LCE-based MEAs deploy, it is equally important that the electrical properties of the device not be compromised by deployment. EIS measurements collected before and after shape change revealed no significant changes in impedance and phase at 1 kHz, suggesting that shape change

did not compromise the conductive traces or insulation [4,48–50]. During the 7 day soak test, the impedance and phase at 1 kHz changed significantly over the first 4 days, consistent with our prior study using substrate-integrated LCE-based MEAs [21], which is likely due to residual debris on electrode sites after fabrication. Impedance values stabilized after day 4 and were well within the range capable of physiological recordings. In addition, the phase at 1 kHz remained primarily capacitive throughout, suggesting that any impedance magnitude change due to saline infiltration was minimal [51]. We also carried out acute neuronal recordings in rat motor cortex using functional 8 channel LCE-based devices with a size-matched silicon host shank. We observed SNR values and the fraction of active electrodes similar to prior studies that performed neuronal recordings at similar depths in rat cortex (18 -53%) [42,43]. In total, our findings demonstrate the feasibility of fabricating an LCE-based MEA capable of in vivo recordings following deployment of > 100 µm, the first such demonstration to be published to date. In addition to neuronal recordings, interest has grown for the use of LCEs in other biomedical applications such as the development of artificial muscles [52-58]. However, to pursue these clinical applications, the LCE-based interface may require actuation in vivo. In this study, we observed deployment of functional LCE-based probes > 100 µm in rat cortex after tissue clearing. To the best of our knowledge, no prior study has demonstrated deployment of LCEs in vivo or the successful implantation of a functionalized LCE-based device.

Our long-term vision is the design and development of a deployable device consisting of a multitude of extremely fine MEA sites from a central implant structure that provides signal processing and multiplexing. Our present work demonstrates that LCEbased deployable intracortical probes are electrochemically stable before and after deployment, capable of recording electrophysiological signals from neurons in vivo, and capable of deploying $> 100 \mu m$ (size of FBR zone) both in agarose and in brain tissue. There are several fabrication and patterning challenges that remain. To ensure deployment greater than 100 μm , the cross-sections of the devices used in this study were much larger than cross-sections typically found in state-of-the-art MEAs [4,50]. Therefore, it will be necessary to optimize LCE-based MEAs to achieve a reduction in the size of the device while maintaining similar deployment distance. This should increase the selectivity of the device and reduce tissue damage caused by insertion. This may potentially be achieved by utilizing LCEs with higher elastic moduli. The use of intrinsic stresses in LCE-based devices offers manufacturability of 3D polymer MEAs without the need for complicated techniques such as thermoforming, which may introduce more failure modes. In addition, it will be necessary to adapt the LCE materials in order to implement the patterning of conductive features with much higher resolution to allow for smaller trace widths and MEA sites as well as a higher channel count. Finally, future work will take advantage of the stimulus-evoked (i.e., heating by electrical current or light) nature of the LCE shape change, rather than relying on PEG coating to maintain a non-deployed state prior to implantation.

Declaration of Competing Interest

The authors declare no conflicts of interest.

Acknowledgments

This research was partially supported by the National Science Foundation under grants No. 1711383 and 1752846 and by the University of Texas at Dallas.

Supplementary materials

Supplementary material associated with this article can be found, in the online version, at doi:10.1016/j.actbio.2020.04.032.

References

- [1] L.R. Hochberg, D. Bacher, B. Jarosiewicz, N.Y. Masse, J.D. Simeral, J. Vogel, S. Haddadin, J. Liu, S.S. Cash, P. Van Der Smagt, J.P. Donoghue, Reach and grasp by people with tetraplegia using a neurally controlled robotic arm, Nature (2012). doi:10.1038/nature11076.
- [2] G. Buzsáki, Large-scale recording of neuronal ensembles, Nat. Neurosci. 7 (2004) 446-451, doi:10.1038/nn1233.
- [3] T.D.Y. Kozai, Z. Gugel, X. Li, P.J. Gilgunn, R. Khilwani, O.B. Ozdoganlar, G.K. Fedder, D.J. Weber, X.T. Cui, Chronic tissue response to carboxymethyl cellulose based dissolvable insertion needle for ultra-small neural probes, Biomaterials (2014), doi:10.1016/j.biomaterials.2014.07.039.
- [4] L. Luan, X. Wei, Z. Zhao, J.J. Siegel, O. Potnis, C.A. Tuppen, S. Lin, S. Kazmi, R.A. Fowler, S. Holloway, A.K. Dunn, R.A. Chitwood, C. Xie, Ultraflexible nanoelectronic probes form reliable, glial scar-free neural integration, Sci. Adv. (2017), doi:10.1126/sciadv.1601966.
- [5] P.R. Patel, K. Na, H. Zhang, T.D.Y. Kozai, N.A. Kotov, E. Yoon, C.A. Chestek, Insertion of linear 8.4µm diameter 16 channel carbon fiber electrode arrays for single unit recordings, J. Neural Eng. (2015), doi:10.1088/1741-2560/12/4/046009.
- [6] G. Guitchounts, J.E. Markowitz, W.A. Liberti, T.J. Gardner, A carbon-fiber electrode array for long-term neural recording, J. Neural Eng. (2013), doi:10.1088/1741-2560/10/4/046016.
- [7] M. Jorfi, J.L. Skousen, C. Weder, J.R. Capadona, Progress towards biocompatible intracortical microelectrodes for neural interfacing applications, J. Neural Eng. (2015), doi:10.1088/1741-2560/12/1/011001.
- [8] R. Biran, D.C. Martin, P.A. Tresco, Neuronal cell loss accompanies the brain tissue response to chronically implanted silicon microelectrode arrays, Exp. Neurol. (2005), doi:10.1016/j.expneurol.2005.04.020.
- [9] B.K. Leung, R. Biran, C.J. Underwood, P.A. Tresco, Characterization of microglial attachment and cytokine release on biomaterials of differing surface chemistry, Biomaterials (2008), doi:10.1016/j.biomaterials.2008.03.045.
- [10] C. Xie, J. Liu, T.M. Fu, X. Dai, W. Zhou, C.M. Lieber, Three-dimensional macroporous nanoelectronic networks as minimally invasive brain probes, Nat. Mater. 14 (2015) 1286–1292, doi:10.1038/nmat4427.
- [11] C. Hassler, T. Boretius, T. Stieglitz, Polymers for neural implants, J. Polym. Sci. Part B Polym. Phys. (2011), doi:10.1002/polb.22169.
- [12] J.K. Nguyen, D.J. Park, J.L. Skousen, A.E. Hess-Dunning, D.J. Tyler, S.J. Rowan, C. Weder, J.R. Capadona, Mechanically-compliant intracortical implants reduce the neuroinflammatory response, J. Neural Eng. (2014), doi:10.1088/1741-2560/ 11/5/056014.
- [13] F. Vitale, D.G. Vercosa, A.V. Rodriguez, S.S. Pamulapati, F. Seibt, E. Lewis, J.S. Yan, K. Badhiwala, M. Adnan, G. Royer-Carfagni, M. Beierlein, C. Kemere, M. Pasquali, J.T. Robinson, Fluidic microactuation of flexible electrodes for neural recording, Nano Lett. 18 (2018) 326–335, doi:10.1021/acs.nanolett.7b04184.
- [14] X. Jiao, Y. Wang, Q. Qing, Scalable fabrication framework of implantable ultrathin and flexible probes with biodegradable sacrificial layers, Nano Lett. (2017), doi:10.1021/acs.nanolett.7b02851.
- [15] D. Egert, K. Najafi, New class of chronic recording multichannel neural probes with post-implant self-deployed satellite recording sites, in: Proceedings of the Sixteenth International Solid-State Sensors, Actuators Microsystems Conference TRANSDUCERS'11, 2011, doi:10.1109/TRANSDUCERS.2011.5969351.
- [16] C. Xie, J. Liu, T.M. Fu, X. Dai, W. Zhou, C.M. Lieber, Three-dimensional macroporous nanoelectronic networks as minimally invasive brain probes, Nat. Mater. (2015), doi:10.1038/nmat4427.
- [17] T.L. Massey, L.S. Kuo, J.L. Fan, M.M. Maharbiz, An actuated neural probe architecture for reducing gliosis-induced recording degradation, IEEE Trans. Nanobiosci. (2019), doi:10.1109/TNB.2019.2905468.
- [18] T.J. White, D.J. Broer, Programmable and adaptive mechanics with liquid crystal polymer networks and elastomers, Nat. Mater. (2015), doi:10.1038/nmat4433.
- [19] R.S. Kularatne, H. Kim, J.M. Boothby, T.H. Ware, Liquid crystal elastomer actuators: synthesis, alignment, and applications, J. Polym. Sci. Part B Polym. Phys. (2017), doi:10.1002/polb.24287.
- [20] J. Küpfer, H. Finkelmann, Nematic liquid single crystal elastomers, Die Makromol. Chem. Rapid Commun. 12 (1991) 717–726, doi:10.1002/marc.1991. 030121211
- [21] R. Rihani, H. Kim, B. Black, R. Atmaramani, M. Saed, J. Pancrazio, T. Ware, Liquid crystal elastomer-based microelectrode array for in vitro neuronal recordings, Micromachines (2018), doi:10.3390/mi9080416.
- [22] Y. Gao, T. Mori, S. Manning, Y. Zhao, A.D. Nielsen, A. Neshat, A. Sharma, C.J. Mahnen, H.R. Everson, S. Crotty, R.J. Clements, C. Malcuit, E. Hegmann, Biocompatible 3D liquid crystal elastomer cell scaffolds and foams with primary and secondary porous architecture, ACS Macro Lett. (2016), doi:10.1021/ acsmacrolett.5b00729.
- [23] C.M. Yakacki, M. Saed, D.P. Nair, T. Gong, S.M. Reed, C.N. Bowman, Tailorable and programmable liquid-crystalline elastomers using a two-stage thiol-acrylate reaction, RSC Adv. (2015), doi:10.1039/c5ra01039j.
- [24] T.H. Ware, M.E. McConney, J.J. Wie, V.P. Tondiglia, T.J. White, Voxelated liquid crystal elastomers, Science 347 (2015) 982–984 (80-.), doi:10.1126/science. 1261019.

- [25] H. Wermter, H. Finkelmann, Liquid crystalline elastomers as artificial muscles, E-Polymers 1 (1) (2001) 1–13, doi:10.1515/epoly.2001.1.1.111.
- [26] A.H. Gelebart, D.J. Mulder, M. Varga, A. Konya, G. Vantomme, E.W. Meijer, L.B.R. Selinger, D.J. Broer, Making waves in a photoactive polymer film, Nature 546 (2017) 632–636, doi:10.1038/nature22987.
- [27] H. Yu, T. Ikeda, Photocontrollable liquid-crystalline actuators, Adv. Mater. (2011), doi:10.1002/adma.201100131.
 [28] M. Chambers, B. Zalar, M. Remškar, S. Žumer, H. Finkelmann, Actuation of liq-
- uid crystal elastomers reprocessed with carbon nanoparticles, Appl. Phys. Lett. (2006), doi:10.1063/1.2404952.
- [29] K. Urayama, Selected issues in liquid crystal elastomers and gels, Macro-molecules (2007), doi:10.1021/ma0623688.
- [30] L.T. De Haan, J.M.N. Verjans, D.J. Broer, C.W.M. Bastiaansen, A.P.H.J. Schenning, Humidity-responsive liquid crystalline polymer actuators with an asymmetry in the molecular trigger that bend, fold, and curl, J. Am. Chem. Soc. (2014), doi:10.1021/ja505475x.
- [31] H. Kim, J. Gibson, J. Maeng, M.O. Saed, K. Pimentel, R.T. Rihani, J.J. Pancrazio, S.V. Georgakopoulos, T.H. Ware, Responsive, 3D Electronics Enabled by Liquid Crystal Elastomer Substrates, ACS Appl. Mater. Interfaces (2019), doi:10.1021/ acsami.9504189.
- [32] S. Zhang, C. Wang, H. Gao, C. Yu, Q. Yan, Y. Lu, Z. Tao, C. Linghu, Z. Chen, K. Xu, J. Song, A Removable Insertion Shuttle for Ultraflexible Neural Probe Implantation with Stable Chronic Brain Electrophysiological Recording, Adv. Mater. Interfaces (2020), doi:10.1002/admi.201901775.
- [33] T. Il Kim, J.G. McCall, Y.H. Jung, X. Huang, E.R. Siuda, Y. Li, J. Song, Y.M. Song, H.A. Pao, R.H. Kim, C. Lu, S.D. Lee, I.S. Song, G. Shin, R. Al-Hasani, S. Kim, M.P. Tan, Y. Huang, F.G. Omenetto, J.A. Rogers, M.R. Bruchas, Injectable, cellular-scale optoelectronics with applications for wireless optogenetics, Science (2013) (80-.), doi:10.1126/science.1232437.
- [34] J. Agorelius, F. Tsanakalis, A. Friberg, P.T. Thorbergsson, L.M.E. Pettersson, J. Schouenborg, An array of highly flexible electrodes with a tailored configuration locked by gelatin during implantation-initial evaluation in cortex cerebri of awake rats, Front. Neurosci. (2015), doi:10.3389/fnins.2015.00331.
- [35] J.M. Boothby, T.H. Ware, Dual-responsive, shape-switching bilayers enabled by liquid crystal elastomers, Soft Matter 13 (2017) 4349–4356, doi:10.1039/ c7sm00541e.
- [36] J.M. Boothby, H. Kim, T.H. Ware, Shape changes in chemoresponsive liquid crystal elastomers, Sens. Actuat. B Chem 240 (2017) 511–518, doi:10.1016/j.snb. 2016.09.004.
- [37] Microsystem Design, 2002. 10.1007/b117574.
- [38] T. Parupudi, R. Rahimi, M. Ammirati, R. Sundararajan, A.L. Garner, B. Ziaie, Fabrication and characterization of implantable flushable electrodes for electric field-mediated drug delivery in a brain tissue-mimic agarose gel, Electrophoresis (2018), doi:10.1002/elps.201800161.
- [39] R. Pomfret, G. Miranpuri, K. Sillay, The substitute brain and the potential of the gel model, Ann. Neurosci. (2013), doi:10.5214/ans.0972.7531.200309.
- [40] S. Budday, G. Sommer, C. Birkl, C. Langkammer, J. Haybaeck, J. Kohnert, M. Bauer, F. Paulsen, P. Steinmann, E. Kuhl, G.A. Holzapfel, Mechanical characterization of human brain tissue, Acta Biomater. (2017), doi:10.1016/j.actbio. 2016.10.036.
- [41] B.S. Elkin, A.I. Ilankovan, B. Morrison, A detailed viscoelastic characterization of the P17 and adult rat brain, J. Neurotrauma (2011), doi:10.1089/neu.2010.1604.
- [42] A.M. Stiller, J. Usoro, C.L. Frewin, V.R. Danda, M. Ecker, A. Joshi-imre, K.C. Musselman, W. Voit, R. Modi, J.J. Pancrazio, B.J. Black, Chronic intracortical recording and electrochemical stability of thiol-ene / acrylate shape memory polymer electrode arrays, Micromachines 9 (2018) 500, doi:10.3390/mi9100500.
- [43] B.J. Black, A. Kanneganti, A. Joshi-Imre, R. Rihani, B. Chakraborty, J. Abbott, J.J. Pancrazio, S.F. Cogan, Chronic recording and electrochemical performance of Utah microelectrode arrays implanted in rat motor cortex, J. Neurophysiol. (2018), doi:10.1152/jn.00181.2018.
- [44] H.U. Dodt, U. Leischner, A. Schierloh, N. Jährling, C.P. Mauch, K. Deininger, J.M. Deussing, M. Eder, W. Zieglgänsberger, K. Becker, Ultramicroscopy: threedimensional visualization of neuronal networks in the whole mouse brain, Nat. Methods (2007), doi:10.1038/nmeth1036.
- [45] Y. Sawa, F. Ye, K. Urayama, T. Takigawa, V. Gimenez-Pinto, R.L.B. Selinger, J.V. Selinger, Shape selection of twist-nematic-elastomer ribbons, Proc. Natl. Acad. Sci. USA (2011), doi:10.1073/pnas.1017658108.
- [46] T.D.Y. Kozai, K. Catt, Z. Du, K. Na, O. Srivannavit, R.U.M. Haque, J. Seymour, K.D. Wise, E. Yoon, X.T. Cui, Chronic In Vivo evaluation of PEDOT/CNT for stable neural recordings, IEEE Trans. Biomed. Eng. 63 (2016) 111–119, doi:10.1109/TBME.2015.2445713.
- [47] M.E. Spira, A. Hai, Multi-electrode array technologies for neuroscience and cardiology, Nat. Nanotechnol. (2013), doi:10.1038/nnano.2012.265.
- [48] S.P. Lacour, S. Benmerah, E. Tarte, J. Fitzgerald, J. Serra, S. McMahon, J. Fawcett, O. Graudejus, Z. Yu, B. Morrison, Flexible and stretchable micro-electrodes for in vitro and in vivo neural interfaces, Med. Biol. Eng. Comput. (2010), doi:10. 1007/s11517-010-0644-8.
- [49] Z. Xiang, S.C. Yen, N. Xue, T. Sun, W.M. Tsang, S. Zhang, L. De Liao, N.V. Thakor, C. Lee, Ultra-thin flexible polyimide neural probe embedded in a dissolvable maltose-coated microneedle, J. Micromech. Microeng. (2014), doi:10.1088/ 0960-1317/24/6/065015.
- [50] S. Guan, J. Wang, X. Gu, Y. Zhao, R. Hou, H. Fan, L. Zou, L. Gao, M. Du, C. Li, Y. Fang, Elastocapillary self-assembled neurotassels for stable neural activity recordings, Sci. Adv. (2019), doi:10.1126/sciadv.aav2842.
- [51] A. Zátonyi, G. Orbán, R. Modi, G. Márton, D. Meszéna, I. Ulbert, A. Pongrácz, M. Ecker, W.E. Voit, A. Joshi-Imre, Z. Fekete, A softening laminar electrode

- for recording single unit activity from the rat hippocampus, Sci. Rep. (2019), doi: 10.1038/s41598-019-39835-6.
- [52] S. Petsch, R. Rix, B. Khatri, S. Schuhladen, P. Müller, R. Zentel, H. Zappe, Smart artificial muscle actuators: liquid crystal elastomers with integrated temperature feedback, Sens. Actuat. A Phys (2015), doi:10.1016/j.sna.2014.10.014.
- [53] H. Wermter, H. Finkelmann, Liquid crystalline elastomers as artificial muscles, E-Polymers 1 (2001) 1–13, doi:10.1515/epoly.2001.1.1.111.
- [54] M.H. Li, P. Keller, M. Antonietti, D. Lacey, R.B. Meyer, Artificial muscles based on liquid crystal elastomers, Philos. Trans. R. Soc. A Math. Phys. Eng. Sci. (2006), doi:10.1098/rsta.2006.1853.
- (2006), doi. 10.1036/15ta.2006.1053.
 [55] A. Buguin, M.H. Li, P. Silberzan, B. Ladoux, P. Keller, Micro-actuators: when artificial muscles made of nematic liquid crystal elastomers meet soft lithography, J. Am. Chem. Soc. (2006), doi:10.1021/ja0575070.
- [56] T. Iii, D. L, P. Keller, J. Naciri, R. Pink, H. Joen, D. Shenoy, B.R. Ratna, Liquid crystal elastomers with mechanical properties of a muscle, Macromolecules (2001).
- [57] S. Schuhladen, F. Preller, R. Rix, S. Petsch, R. Zentel, H. Zappe, Iris-like tunable aperture employing liquid-crystal elastomers, Adv. Mater. (2014), doi:10.1002/ adma.201402878.
- [58] H. Zeng, O.M. Wani, P. Wasylczyk, R. Kaczmarek, A. Priimagi, Self-Regulating Iris Based on Light-Actuated Liquid Crystal Elastomer, Adv. Mater. (2017), doi:10.1002/adma.201701814.